

GRB 130606A AS A PROBE OF THE INTERGALACTIC MEDIUM AND THE INTERSTELLAR MEDIUM IN A STAR-FORMING GALAXY IN THE FIRST GYR AFTER THE BIG BANG

RYAN CHORNOCK¹, EDO BERGER¹, DEREK B. FOX², RAGNHILD LUNNAN¹, MARIA R. DROUT¹, WEN-FAI FONG¹, TANMOY LASKAR¹, AND KATHERINE C. ROTH³

Draft version October 1, 2018

ABSTRACT

We present high signal-to-noise ratio Gemini and MMT spectroscopy of the optical afterglow of the gamma-ray burst (GRB) 130606A at redshift $z=5.913$, discovered by *Swift*. This is the first high-redshift GRB afterglow to have spectra of comparable quality to those of $z \approx 6$ quasars. The data exhibit a smooth continuum at near-infrared wavelengths that is sharply cut off blueward of 8410 Å due to absorption from Ly α at redshift $z \approx 5.91$, with some flux transmitted through the Ly α forest between 7000–7800 Å. We use column densities inferred from metal absorption lines to constrain the metallicity of the host galaxy between a lower limit of $[\text{Si}/\text{H}] \gtrsim -1.7$ and an upper limit of $[\text{S}/\text{H}] \lesssim -0.5$ set by the non-detection of S II absorption. We demonstrate consistency between the dramatic evolution in the transmission fraction of Ly α seen in this spectrum over the redshift range $z = 4.9$ to 5.85 with that previously measured from observations of high-redshift quasars. There is an extended redshift interval of $\Delta z=0.12$ in the Ly α forest at $z=5.77$ with no detected transmission, leading to a 3σ upper limit on the mean Ly α transmission fraction of $\lesssim 0.2\%$ (or $\tau_{\text{GP}}^{\text{eff}}(\text{Ly}\alpha) > 6.4$). This is comparable to the lowest-redshift Gunn-Peterson troughs found in quasar spectra. Some Ly β and Ly γ transmission is detected in this redshift window, indicating that it is not completely opaque, and hence that the IGM is nonetheless mostly ionized at these redshifts. We set a 2σ upper limit of 0.11 on the neutral fraction of the IGM at the redshift of the GRB from the lack of a Ly α red damping wing, assuming a model with a constant neutral density. GRB 130606A thus for the first time realizes the promise of GRBs as probes of the first galaxies and cosmic reionization.

Subject headings: gamma-ray bursts: individual (GRB 130606A) — intergalactic medium — dark ages, reionization, first stars — galaxies: abundances

1. INTRODUCTION

Observations of Gunn-Peterson absorption troughs (Gunn & Peterson 1965) detected in the spectra of quasars at redshifts $z \approx 6$ (Becker et al. 2001) have been interpreted as representing the end stages of the reionization of the intergalactic medium (IGM; e.g., Fan et al. 2006b). However, the polarization of the cosmic microwave background radiation implies a higher typical redshift for reionization (Hinshaw et al. 2012). These observations indicate that reionization was likely a complex process that occurred over a range in cosmic times with strong local variations. Long-duration gamma-ray bursts (GRBs) are produced by the deaths of massive stars (e.g., Woosley & Bloom 2006) and offer the promise of being important probes of this process with their highly luminous afterglows being detectable to large redshifts (Lamb & Reichart 2000).

The most useful probe of the IGM opacity at high redshifts has been Ly α seen in absorption of quasars, but quasars have some disadvantages as probes. At low redshift, quasar measurements can interpolate across absorptions in the Ly α forest, but at higher redshift the continuum is so highly absorbed that the proper level has

to be inferred. The smooth power-law spectra of GRB afterglows are intrinsically much simpler than the complicated spectra of quasars, which have emission lines and sometimes broad absorption. Aside from practical matters, quasars may not be unbiased probes of the high-redshift universe. The ultraviolet (UV) emission from quasars ionizes the region around them through the proximity effect. In addition, Mesinger (2010) has argued that the highest-redshift quasars are hosted by massive dark matter halos that are highly biased tracers of the underlying matter distribution. Even ignoring the ionizing radiation from the quasar, he finds that typical high-redshift quasars are located in regions that are overionized relative to the average due to the associated large-scale structure. GRBs are associated with sites of massive-star formation and will be more widely distributed at high redshift in galaxies of lower masses (Tanvir et al. 2012) than the rare massive black holes needed to power the most luminous quasars.

There are now only three spectroscopically-confirmed GRBs at $z > 6$ despite active follow-up efforts of suspected high- z bursts: GRB 050904 at $z=6.295$ (Kawai et al. 2006; Haislip et al. 2006; Totani et al. 2006), GRB 080913 at $z=6.733$ (Greiner et al. 2009; Patel et al. 2010), and GRB 090423 at $z \approx 8.2$ (Tanvir et al. 2009; Salvaterra et al. 2009). In addition, GRB 090429B has a photometric redshift of ~ 9.4 (Cucchiara et al. 2011). These objects have proven the existence of GRBs at these early epochs, and are beginning to demonstrate the application of GRBs to stud-

¹ Harvard-Smithsonian Center for Astrophysics, 60 Garden Street, Cambridge, MA 02138, USA; rchnock@cfa.harvard.edu

² Department of Astronomy and Astrophysics, Pennsylvania State University, 525 Davey Laboratory, University Park, PA 16802, USA

³ Gemini Observatory, 670 North Aohoku Place, Hilo, HI 96720, USA

ies of star formation in the early universe (Tanvir et al. 2012). However, despite their promise as bright probes (Lamb & Reichart 2000), high- z GRB afterglow studies of the IGM to date (Totani et al. 2006; Gallerani et al. 2008; Patel et al. 2010) have been hindered by the limited signal-to-noise ratio (S/N) of the available spectra. This has now changed with the discovery of GRB 130606A and our follow-up observations.

The *Swift* Burst Alert Telescope (BAT) triggered on GRB 130606A on 2013 June 6 at 21:04:39 (all dates and times are UT; Ukwatta et al. 2013). The high-energy emission was extended, with a duration of $T_{90} = 277 \pm 19$ s as seen by BAT (Barthelmy et al. 2013), firmly establishing GRB 130606A as a member of the long-duration population of GRBs. Subsequent ground-based followup observations located an optical transient (e.g., Jelinek et al. 2013; Xu et al. 2013a) that was brighter in the near-infrared (NIR; Nagayama 2013; Virgili et al. 2013). Initial spectroscopy from the Gran Telescopio Canarias (Castro-Tirado et al. 2013a) revealed that the afterglow redshift was $z \approx 6.1$, which was subsequently refined to $z = 5.913$ by several groups, including ours (Castro-Tirado et al. 2013b; Lunnan et al. 2013; Xu et al. 2013b).

We present an analysis of the optical spectra of the afterglow of GRB 130606A, the first high-redshift GRB spectra to be comparable in quality to those of typical $z \approx 6$ quasars. In section 2, we describe the data acquisition and reduction. We analyze the metal absorption lines from the host galaxy and intervening IGM systems in section 3, and set constraints on the abundances in the ISM of the $z = 5.913$ host galaxy. In section 4, we measure the properties of the Ly α , Ly β , and Ly γ absorption of the IGM and compare to previous observations of high-redshift quasars. We discuss the implications in section 5.

2. OBSERVATIONS

We observed the afterglow of GRB 130606A starting at 04:04 on 2013 June 7 using the Blue Channel spectrograph (Schmidt et al. 1989) on the 6.5-m MMT. We obtained a set of four 1200 s spectra as GRB 130606A rose from airmass 1.22 to 1.08 with a midpoint time of 04:45 ($\Delta t = 7.68$ hr after the BAT trigger). The 832 lines/mm grating and LP530 order-blocking filter were used to cover the range 7460–9360 Å. Our 1''-wide slit gave a spectral resolution of 2.0 Å full width at half-maximum (FWHM) and was oriented at the parallactic angle (Filippenko 1982) to reduce effects of differential atmospheric dispersion. We acquired the source by taking advantage of the excellent pointing of the MMT to offset from a nearby bright star to the coordinates for the afterglow rapidly distributed by Xu et al. (2013a). These coordinates are somewhat offset from the precise radio position given by Laskar et al. (2013), possibly indicating that the object was not fully in the slit.

We subsequently obtained four 1800 s observations of GRB 130606A using the Gemini Multi-Object Spectrograph (GMOS; Hook et al. 2004) on the 8-m Gemini-North telescope, with a midpoint of 10:17 on 2013 June 7 ($\Delta t = 13.1$ hr). The spectra were obtained in nod-and-shuffle mode (Glazebrook & Bland-Hawthorn 2001) with the R400 grating and RG610 order-blocking filter. We took advantage of the new red-sensitive deep depletion

detectors to use a grating setup with coverage longward of 1 μ m. The excellent seeing (0.5–0.7'') over the course of observations allowed us to have a spectral resolution of ~ 5 Å over the observed spectral range of 6200–10500 Å. The grating angle was adjusted by 50 Å between the second and third observations to fill in CCD chip gaps. The 1''-wide slit was oriented at a position angle of 90°, but the airmass was low (< 1.1).

We use IRAF⁴ to perform basic two-dimensional image processing and extract the spectra after removal of cosmic rays (van Dokkum 2001). We apply flux calibrations and correct for telluric absorption using our own IDL procedures. Two aspects of the GMOS data reduction require special attention. The first is that because Gemini does not generally obtain standard stars at the time of observations, the variable atmospheric H₂O absorption strength can lead to errors in the correction for telluric absorption in the strong band near 9400 Å. We obtain archival observations of the standard star BD+28 4211 and are careful to scale the H₂O portion of the telluric correction separately from the correction at the O₂ absorption bands.

The second effect is that the Gemini data were taken in nod-and-shuffle mode. We reduce the Gemini data with two methods, once after applying the expected pairwise subtraction of the data from the two nod positions and once ignoring the nod pairs and treating each spectrum as a normal long-slit observation. The first method leads to better control of systematic sky subtraction errors produced by flat fielding errors and bright night sky emission lines, but comes at a cost of a factor of $\sqrt{2}$ increase in the Poisson errors in night sky dominated portions of the spectrum. In both cases, we align and stack the two-dimensional frames taken with the same grating tilt angle prior to spectral extraction. The two reductions are highly consistent, so we splice them together at 8780 Å, using the second method at shorter wavelengths to obtain the best S/N, while the nod-and-shuffle reduction was used at longer wavelengths where the systematic residuals from sky subtraction are otherwise problematic.

We rebinned the calibrated one-dimensional spectra for each GMOS grating setup to a common vacuum heliocentric wavelength scale and combined them on a pixel-by-pixel basis, weighted by the inverse variance⁵. The final MMT and GMOS spectra are plotted in Figure 1. The absolute flux scale is uncertain, both due to our use of an archival standard star at Gemini and the fading of the afterglow that is clearly evident during the observations. Both spectra have been corrected for $E(B - V) = 0.02$ mag of Galactic extinction (Schlafly & Finkbeiner 2011). In the continuum between 8500 and 8600 Å, the MMT spectrum has a median S/N per 0.71 Å pixel of ~ 10 , while for the Gemini data the median S/N per 1.38 Å pixel is ~ 80 and decreasing to longer wavelengths.

Before proceeding further, we normalize the spectra by fitting a power-law continuum to wavelength intervals in

⁴ IRAF is distributed by the National Optical Astronomy Observatories, which are operated by the Association of Universities for Research in Astronomy, Inc., under cooperative agreement with the National Science Foundation.

⁵ We note that the sky is sufficiently bright that we are not in the regime pointed out by White et al. (2003) where Poisson weighting biases the resulting flux level near zero counts.

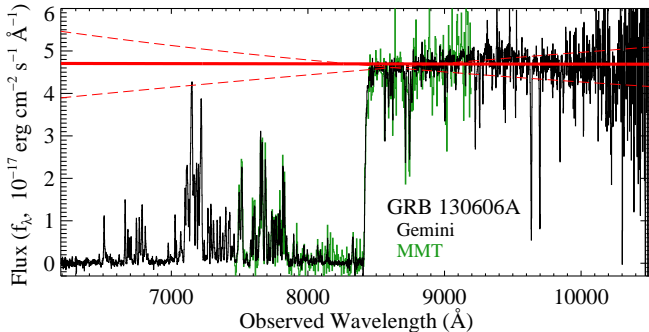


Figure 1. Spectra of the optical afterglow of GRB 130606A from MMT/Blue Channel (green) and Gemini-N/GMOS (black), demonstrating impressive consistency after application of an arbitrary multiplicative scale factor. The noisier MMT spectrum has been binned up by a factor of 6 for display purposes. The solid red line shows a best-fit power law to line-free regions of the continuum. The two dashed red lines show hypothetical extreme systematic variations around the best-fit value. See Section 4.1 for details.

the Gemini spectrum redward of the Ly α break devoid of strong absorption lines. The best-fit continuum is shown as the thick red line and has a slope of $f_\lambda \propto \lambda^{-0.01 \pm 0.04}$, although some curvature relative to a pure power law is evident. We divide both spectra by this continuum in all subsequent analysis.

3. ISM PROPERTIES OF A STAR-FORMING GALAXY AT $z=5.913$

The two spectra from different instruments presented in Figure 1 are highly consistent with each other. Both show a flat continuum (in f_λ) at long wavelengths that drops sharply down to zero between 8435 and 8405 Å; flux detected blueward of 8405 Å is largely limited to wavelength intervals between 6500 and 7850 Å. This is indicative of absorption induced by the host galaxy at redshift $z \approx 5.91$ and the Ly α forest at lower redshift.

The normalized GMOS spectrum, displayed in Figure 2, exhibits numerous absorption lines redward of Ly α that arise in the host galaxy and intervening systems. We fit a local continuum and single Gaussian profile to each absorption line in both the Gemini and MMT spectra and list the results in Table 1. The quoted uncertainties in line centroids and equivalent widths (EW) do not include continuum placement uncertainties. We are able to confidently detect N V, Si II, Si II*, O I, O I*, C II, C II*, and Si IV from the host galaxy, as well as the red wing of Ly α absorption at a similar redshift. A weighted average of the narrow, unblended, low-ionization lines gives a redshift for GRB 130606A of $z = 5.9134$, a value which we adopt throughout this paper. The presence of fine-structure lines at this redshift identifies it as that of the GRB because the lower levels for these transitions are not normally populated unless pumped by the UV emission from the GRB afterglow (Prochaska et al. 2006; Vreeswijk et al. 2007).

In addition to absorption from the interstellar medium (ISM) of the host galaxy, we detect absorption from at least four intervening lower-redshift systems. Xu et al. (2013b) previously reported two absorption systems at $z = 2.310$ and 3.451 in X-Shooter spectra. We confirm the existence of the first one through absorption from Mg II and Fe II at an average redshift of $z = 2.3105 \pm 0.0001$. We do not see the system at $z = 3.451$,

although no strong absorption lines from it are expected in our observed wavelength range. In addition, we detect at least three more intervening systems, at weighted average redshifts of $z = 2.5207 \pm 0.0005$, 4.647 ± 0.001 , and 5.806 ± 0.001 . The $z=5.806$ O I/C II/Si II system is particularly interesting in light of recent observational work to find similar systems at these redshifts to probe metal enrichment of the IGM associated with reionization (Becker et al. 2011). We note that C IV $\lambda 1548$ from the $z=4.647$ system completely overlaps the Si II* $\lambda 1265$ absorption from the host and that weak Fe II $\lambda 2586$ at $z=2.3105$ is also likely blended with N V $\lambda 1239$.

One important advantage of the MMT data is that the host absorption lines are generally resolved, while the IGM metal lines are not. We show some unblended line profiles in Figure 3. The Fe II and Si II lines from lower-redshift absorbers have FWHMs consistent with the spectral resolution of ~ 2 Å. However, the host Si II $\lambda 1260$ absorption has a FWHM equivalent to ~ 120 km s $^{-1}$ after subtraction of the instrumental width in quadrature. Most of the host absorption lines appear to be consistent with a single absorption component, but the N V lines are both blueshifted relative to the low-ionization lines and have flat-bottomed profiles. They exhibit absorption spread across ~ 200 km s $^{-1}$, which is unusually broad for N V absorption in GRB afterglows (Prochaska et al. 2008). The Gemini data cannot clearly resolve these features although some variation in FWHM is apparent. In particular, the Si IV doublet shows some structure, with the stronger $\lambda 1394$ line exhibiting a blue wing extending out to a blueshift of ~ 300 km s $^{-1}$. The N V and Si IV profiles probably reflect absorption in a wind or outflow from the host galaxy.

The sharp cutoff of flux between 1215 and 1220 Å due to the wing of Ly α absorption in the host is indicative of a low hydrogen column density ($\log(N_{\text{HI}}) < 20.3$; all reported columns are in units of cm $^{-2}$) in the host galaxy. A fit to the hydrogen column in the GMOS spectrum gives a best fit redshift of $z=5.913 \pm 0.001$, in excellent agreement with the results from the narrow metal lines, and $\log(N_{\text{HI}})=19.93 \pm 0.07$, which we adopt in the subsequent analysis. A fit to the MMT spectrum with the redshift fixed gives a consistent value of $\log(N_{\text{HI}})=19.99$. This value is rather low for a GRB host galaxy (Jakobsson et al. 2006), as it falls below the cutoff of $\log(N_{\text{HI}})=20.3$ for a damped Ly α system (DLA). In the compilation of hydrogen column measurements of $z > 4$ GRB host galaxies presented by Thöne et al. (2013), only 1 out of 12 objects (GRB 080913) has a lower $\log(N_{\text{HI}})$ of 19.84 (Greiner et al. 2009; Patel et al. 2010).

We set a lower limit to the metallicity by converting our absorption line measurements into column densities of the metal ions. In the optically-thin limit, the column N_X of a given ion is given by

$$\log(N_X) = 1.23 \times 10^{20} \text{cm}^{-2} \frac{EW_r(\text{Å})}{\lambda_r(\text{Å})^2 f_{ij}}, \quad (1)$$

where λ_r and EW_r are the wavelength and equivalent width of the transition in the rest frame, respectively, while f_{ij} is the oscillator strength. We use the atomic data collected by Prochaska et al. (2007), and report the results in the rightmost column of Table 1.

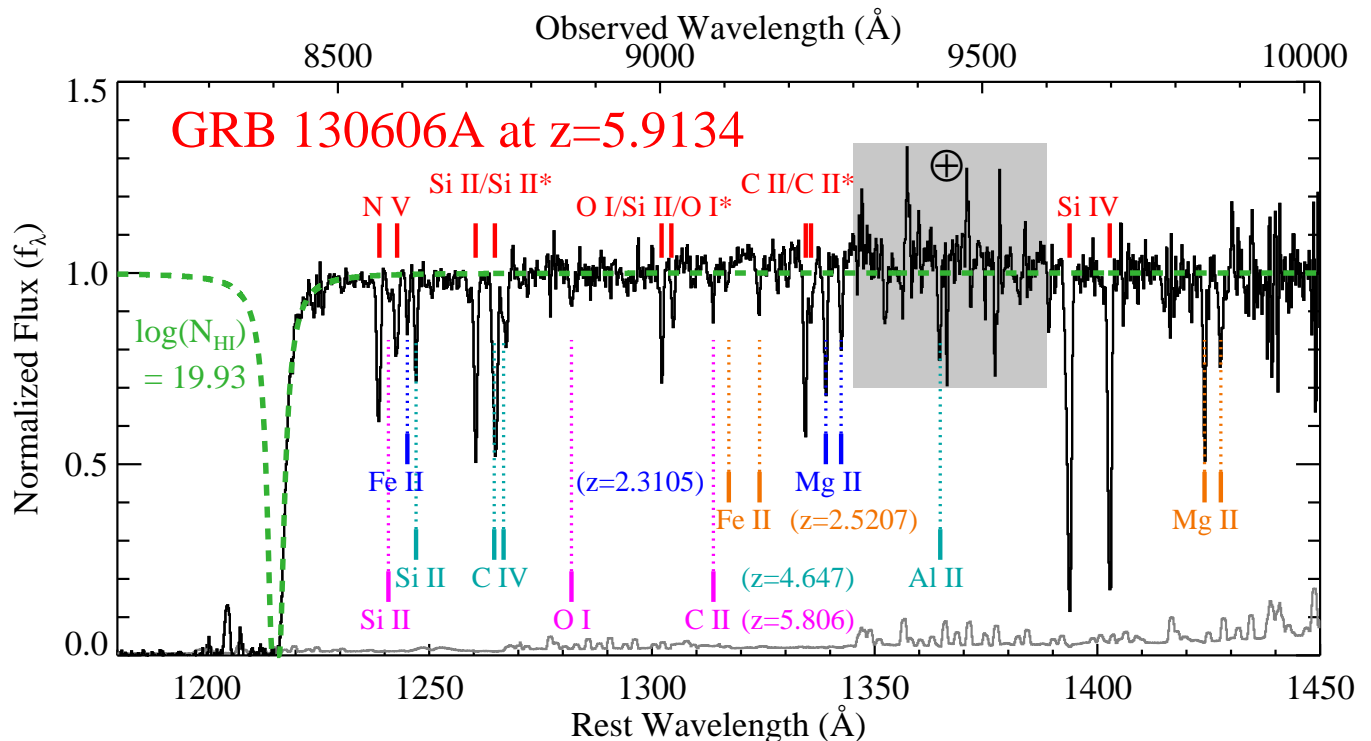


Figure 2. GMOS spectrum of GRB 130606A with prominent absorption lines labeled. Red lines and text identify absorption from the host galaxy at $z = 5.913$. The green dashed line marks a fit to the Ly α line at this redshift, with $\log(N_{\text{HI}}) = 19.93$. The dramatic cutoff in flux at $\lambda < 1200$ Å caused by Ly α at lower redshift is also apparent. At least four intervening absorption systems are present at lower redshift and are labeled in different colors with their redshifts identified. The gray box with the \oplus symbol marks the region possibly containing residuals from the correction for telluric H $_2$ O absorption. The gray line at the bottom is the error spectrum.

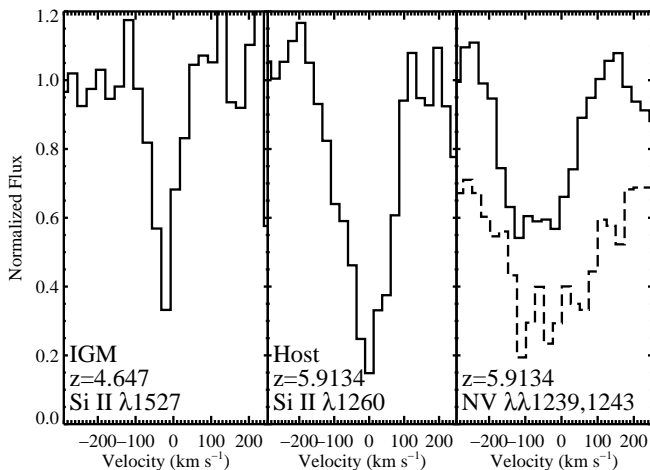


Figure 3. Absorption line profiles in our MMT spectrum. The left panel shows unresolved Si II $\lambda 1527$ absorption from a foreground absorber (FWHM ≈ 67 km s $^{-1}$). The middle panel shows the Si II $\lambda 1260$ absorption from the host, with intrinsic FWHM ≈ 120 km s $^{-1}$. The right panel shows the blueshifted and broader N V doublet absorption from the host, with the $\lambda 1243$ profile shifted downward by 0.4 units. N V $\lambda 1239$ is possibly blended with Fe II $\lambda 2586$ from the $z=2.3105$ foreground absorber, but the profile is fairly consistent with the unblended $\lambda 1243$.

The numbers we present are lower limits to the column density because we make the assumption that all lines are optically thin. This is clearly wrong for the deep Si IV doublet and may be in error for other transitions as well (e.g., the Si II $\lambda 1260$ profile in Figure 3). High-resolution spectroscopy of GRB afterglows has revealed that the

line profiles can have deep saturated cores on top of absorption from lower columns. These saturation effects lead to systematic biases in metallicity measurements for GRB hosts (Prochaska 2006), but the errors incurred are in the direction of making the observed columns too low. We can also take some confidence from the fact that our inferred columns are completely consistent between the GMOS data and the MMT data, which have a factor ~ 3 higher spectral resolution. In fact, our MMT resolution is $R = \lambda/\Delta\lambda \approx 4500$, approaching the moderate resolution of spectrographs such as ESI at Keck or X-Shooter at VLT. In addition, ionization and dust depletion effects can cause us to underestimate the column densities of some elements.

With those caveats in mind, we use the derived columns in Table 1, our value for $\log(N_{\text{HI}})$ from the fit to the wing of Ly α absorption, and the solar photospheric abundances of Asplund et al. (2009) to constrain the metallicity of the host galaxy of GRB 130606A. High-ionization species such as Si IV and N V are not useful for a metallicity analysis as they trace more heavily ionized gas that may not contribute to $\log(N_{\text{HI}})$, as well as in this case having clearly different velocity distributions from the narrow lines (as described above). This leaves O I, C II, and Si II as possible tracers, in addition to their excited fine-structure transitions. In the MMT data, we measure $[\text{O}/\text{H}] \approx -2.0$ for O I $\lambda 1302$ only. The Gemini spectrum has a similar O I column, but also exhibits absorption⁶ from O I*. The combined oxygen abundance

⁶ This line is blended with Si II $\lambda 1304$, but we ascribe it com-

Table 1
Absorption Lines in GRB 130606A Spectra

λ_{obs} (Å)	Line ID	λ_{rest} (Å)	Redshift	EW_r (Å) ^a	$\log(N_X, \text{cm}^{-2})^b$
MMT spectrum					
8562.44±0.32	N V	1238.82	5.9118±0.0003	0.37±0.06	14.24±0.07
8590.87±0.41	N V	1242.80	5.9125±0.0003	0.26±0.07	14.39±0.11
8607.94±0.16	Fe II	2600.17	2.3105±0.0001	0.21±0.07	13.16±0.14
8620.67±0.19	Si II	1526.71	4.6466±0.0001	0.23±0.07	13.94±0.13
8703.00±0.42	Unknown ^c	0.76±0.36	...
8713.65±0.15	Si II	1260.42	5.9133±0.0001	0.50±0.06	13.55±0.05
8744.28±0.32	Si II* ^d	1264.74	5.9139±0.0003	0.59±0.08	13.67±0.06
...	+C IV ^d	1548.20	(4.647)		
8759.56±1.05	C IV	1550.77	4.6485±0.0007	0.36±0.13	14.25±0.16
9002.73±0.34	O I	1302.17	5.9136±0.0003	0.32±0.12	14.64±0.16
Gemini spectrum					
8563.33±0.05	N V	1238.82	5.9125±0.0001	0.38±0.01	14.25±0.01
8580.07±0.40	Si II	1260.42	5.8073±0.0003	0.05±0.01	12.53±0.10
8590.94±0.12	N V	1242.80	5.9125±0.0001	0.21±0.01	14.30±0.02
8608.02±0.13	Fe II	2600.17	2.3106±0.0001	0.23±0.02	13.21±0.04
8621.13±0.10	Si II	1526.71	4.6469±0.0001	0.24±0.02	13.97±0.03
...	S II	1250.58	(5.9134)	$\lesssim 0.04^e$	$\lesssim 14.7$
...	S II	1253.81	(5.9134)	$\gtrsim 0.05$	$\gtrsim 14.6$
8703.51±0.40	Unknown ^c	0.44±0.09	...
8714.09±0.04	Si II	1260.42	5.9136±0.0001	0.43±0.01	13.48±0.01
8744.31±0.05	Si II* ^d	1264.74	5.9139±0.0001	0.60±0.01	13.67±0.01
...	+C IV ^d	1548.20	(4.647)		
8759.78±0.28	C IV	1550.77	4.6487±0.0002	0.29±0.03	14.15±0.04
8862.76±0.47	O I	1302.17	5.8062±0.0004	0.10±0.02	14.12±0.09
9003.10±0.19	O I	1302.17	5.9139±0.0001	0.22±0.03	14.47±0.05
9020.18±0.31	O I* ^d	1304.86	5.9127±0.0002	0.12±0.02	14.25±0.08
...	+Si II ^d	1304.37	(5.9134)		
9082.33±0.29	C II	1334.53	5.8056±0.0002	0.08±0.02	13.62±0.10
9103.74±0.64	Fe II	2586.65	2.5195±0.0002	0.10±0.04	13.40±0.17
9153.45±0.33	Fe II	2600.17	2.5203±0.0001	0.24±0.04	13.23±0.07
9225.28±0.11	C II	1334.53	5.9127±0.0001	0.35±0.02	14.24±0.03
9234.04±0.42	C II*	1335.71	5.9132±0.0003	0.18±0.03	14.01±0.07
9257.06±0.11	Mg II	2796.35	2.3104±0.0001	0.66±0.04	13.19±0.03
9281.16±0.16	Mg II	2803.53	2.3105±0.0001	0.41±0.04	13.28±0.04
9433.75±0.17	Al II	1670.79	4.6463±0.0001	0.27±0.03	12.76±0.05
9635.33±0.07	Si IV	1393.76	5.9132±0.0001	1.05±0.03	14.06±0.01
9698.09±0.10	Si IV	1402.77	5.9135±0.0001	0.86±0.04	14.27±0.02
9845.29±0.15	Mg II	2796.35	2.5208±0.0001	0.65±0.06	13.18±0.04
9870.25±0.62	Mg II	2803.53	2.5206±0.0002	0.44±0.11	13.31±0.11

^a Rest frame

^b Lower limit due to optically-thin assumption

^c EW for unidentified lines are in observer frame

^d Redshifts and column densities are estimated assuming that the stronger component of blend dominates

^e Upper limits are 3σ

in those data is $[\text{O}/\text{H}] \approx -1.95$. The formal uncertainties for these abundance measurements are ~ 0.1 dex, but the systematic errors clearly dominate. Adding the C II and C II* columns from GMOS gives a similar value of $[\text{C}/\text{H}] \approx -1.9$. Determining the silicon column is a little more challenging. The foreground C IV $\lambda 1548$ absorption coincides with the strongest Si II* absorption line. We correct the Si II* $\lambda 1265$ observed-frame EW value for C IV by subtracting an observed-frame EW of $\lambda 1548$ equal to that measured for $\lambda 1551$ and recalculate the column. The exact correction factor has only a small effect on the final result. Combining the Si II and corrected Si II* columns gives a consistent estimate of $[\text{Si}/\text{H}] \approx -1.7$ in both the MMT and Gemini spectra.

pletely to O I*, which is more consistent with the central wavelength of the absorption line.

As described before, our measurements are all lower limits because of dust depletion and the lack of constraints on other ionization stages of the same elements. However, we can also set an upper limit on the metallicity from the non-detection of S II lines. Sulfur has proven useful in previous studies of GRB host galaxies at high redshift (e.g., Kawai et al. 2006; Berger et al. 2006; Price et al. 2007) because the weak S II lines near 1250 Å are not likely to be saturated and sulfur does not deplete onto dust grains (Savage & Sembach 1996). An unidentified absorption line near 8703 Å in the blue wing of Si II $\lambda 1260$ is near the expected position of S II $\lambda 1259.52$ at the redshift of GRB 130606A, but formally the centroid is more than 10σ away from the correct wavelength, so we regard it as a non-detection. In addition, an implied S II column that large should also produce $\lambda 1254$ absorption that is not observed. We estimate observed-frame

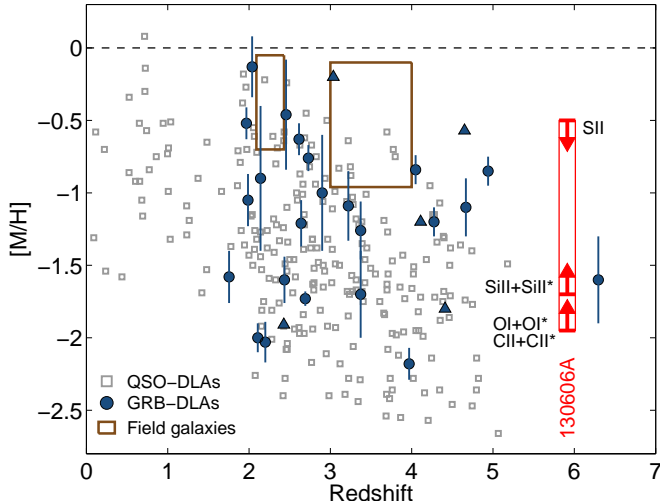


Figure 4. Abundance estimates for the host of GRB 130606A compared to DLA systems in both GRB host galaxies and quasars (Rafelski et al. 2012; Thöne et al. 2013). The brown boxes represent the range in metallicity for star-forming 10^9 – $10^{11} M_{\odot}$ galaxies at $z \approx 2.3$ (Erb et al. 2006) and $z \approx 3.1$ (Mannucci et al. 2009). These results unavoidably conflate measurements using a number of different tracers (e.g., oxygen emission lines in the field galaxies and metal absorption lines in the DLA samples).

EW 3σ upper limits of $\sim 0.3 \text{ \AA}$ for any absorption line near S II $\lambda\lambda 1250, 1254$. These translate into an upper limit on the metallicity of $[S/H] \lesssim -0.5$.

We compare these metallicity constraints for GRB 130606A to abundance measurements for DLA systems in both GRB host galaxies (Thöne et al. 2013) and quasar absorption systems (Rafelski et al. 2012) in Figure 4. We also show the ranges reported in star-forming field galaxy samples in the mass range of 10^9 – $10^{11} M_{\odot}$ at two different redshifts of $z \approx 2.3$ and $z \approx 3.1$ (Erb et al. 2006; Mannucci et al. 2009). The metallicity range for GRB 130606A is at the low end of the dispersion in field galaxy samples at lower redshift, but comparable to the GRB DLA sample.

The point in Figure 4 at $z = 6.295$ from GRB 050904 (Kawai et al. 2006) is of special interest because it represents the most complete abundance analysis of a galaxy at a redshift comparable to GRB 130606A. Kawai et al. (2006) measured the abundance pattern using the exact same lines we use here, except that they detect the S II lines, so systematic issues due to different tracers are minimized. They found $[C/H] \approx -2.4$, $[O/H] \approx -2.3$, $[Si/H] \approx -2.6$, and $[S/H] \approx -1.0$. In comparison with our results from above, the individual numbers are all ~ 0.5 dex higher in the host of GRB 130606A than in that of GRB 050904, likely indicating a metallicity difference of about that magnitude with a similar depletion pattern. It is interesting to note that even at these high redshifts, the ISMs of these star-forming galaxies show clear evidence of chemical enrichment.

4. OPACITY OF THE IGM AT $z \approx 5 - 6$

The spectra we present in Figures 1 and 2 exhibit a well-detected NIR continuum that drops to near zero at 8400 \AA , but then slowly rises to a peak near 7100 \AA before turning over and dropping off blueward of that. This continuum slope in the absorbed part of the spectrum represents real evolution in the optical depth of the Ly α

forest over the redshift range $5 < z < 6$. The very high S/N of our data allow us to place constraints on the opacity of the IGM to Ly α that are comparable to those from individual high-redshift quasars.

We divide our GMOS spectrum by the best-fit continuum marked on Figure 1 and then display the spectrum in Figure 5 with the wavelength scale converted to redshift relative to Ly α , Ly β , and Ly γ . The transmitted flux is clearly broken up into a “picket fence” of individual windows of transmission through the Ly α forest. These windows are rare at $z \approx 5.8$, but become increasingly common at lower redshift until at $z < 5$ they start to overlap. Figure 1 demonstrates the consistency of these windows of transmission in two spectra of different resolutions.

Comparison of the three Lyman-series transitions shows that the pattern of transmission windows is generally the same over the limited overlap region, with the weaker higher-order lines having greater transmission than Ly α , as expected. There are two interesting exceptions. The first is that there is a weak window of transmission present near $z \approx 5.803$ in both Ly β and Ly γ , but not Ly α , in a redshift interval that is otherwise fairly dark. This is intriguingly close to the redshift of the $z=5.806$ system that we detect in metal lines, indicating a moderate local increase in ionization (but not enough for Ly α to become transparent) correlated with the same large scale structure hosting the absorber. Spatial correlations between metal enrichment and ionization are predicted to be sensitive probes of the reionization process and the pollution of the IGM by the earliest galaxies (Oh 2002; Furlanetto & Loeb 2003; Becker et al. 2011).

Second, there is a clear transmission window present in both Ly α and Ly γ between $z=5.69$ – 5.70 that is missing from Ly β . Although this region falls squarely in the atmospheric B band, the spectrum has been corrected for telluric absorption and some flux might be expected to be detected in data of this quality. Instead, we note that the Ly α absorption associated with the $z = 4.647$ system we detect in metal lines would lie at exactly this redshift relative to Ly β . This serves as a cautionary reminder that some absorption we attribute to the Lyman series can be due to either metal lines or Ly α at lower redshift.

We now compare the transmission along the line of sight to this high-redshift GRB with previous studies using high-redshift quasars as background light sources. Songaila (2004) used high-quality moderate and high-resolution Keck spectra of a sample of quasars to measure the mean transmission of Ly α . She computed the average transmission in 15 \AA bins in the rest frame of each quasar between 1080 and 1185 \AA (limits chosen to avoid Ly β and Ly α proximity effects from each quasar) and measured the mean and its variation along different lines of sight. The thick solid line in Figure 6 marks the mean transmission measured from the quasars and the thick gray band marks the observed minimum and maximum values in her sample. We measure the transmission in wavelength bins of the same size over the interval 1035 – 1200 \AA . The low $\log(N_{\text{HI}})$ of the host of GRB 130606A allows us to measure the IGM opacity as close to the host redshift as 1200 \AA without interference from the blue wing of Ly α (cf. Figure 2). The red boxes in Figure 6 mark our measurements. The formal error bars are far smaller than the

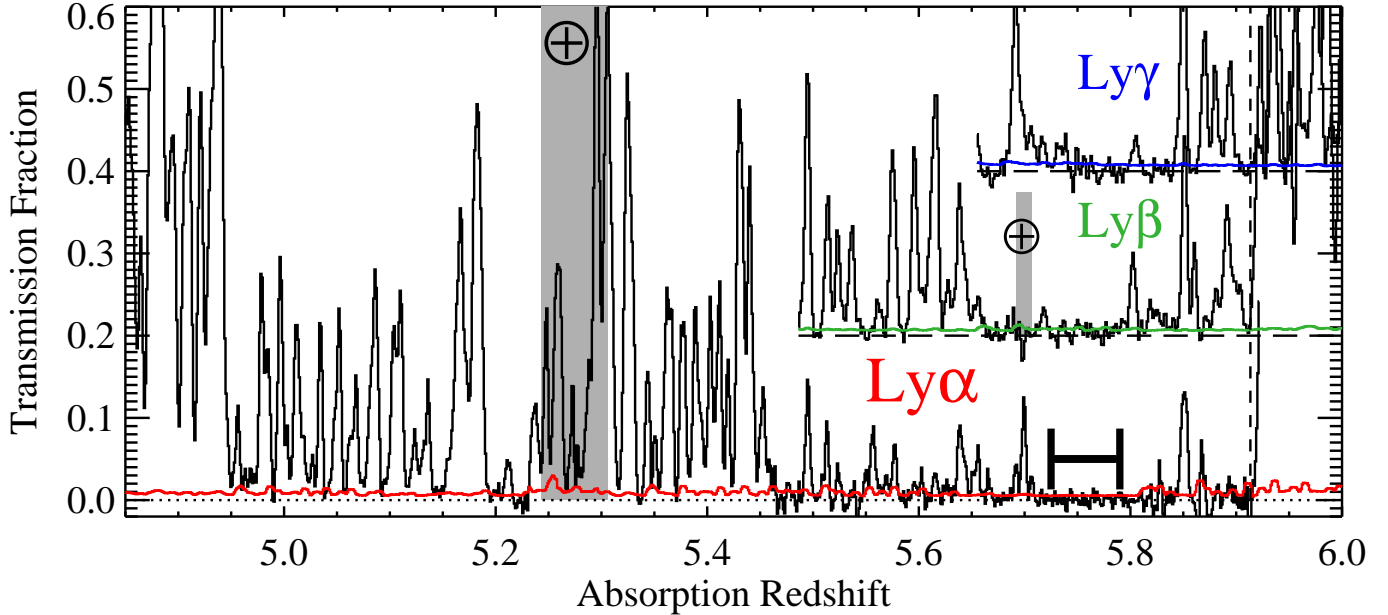


Figure 5. Transmission fraction of Lyman-series transitions versus redshift. The spectrum corresponding to $\text{Ly}\beta$ has been shifted upward by 0.2 and that of $\text{Ly}\gamma$ by 0.4, with the horizontal dashed lines marking the new zero levels. The red, green, and blue lines represent the 1σ uncertainties about zero. The gray bars with \oplus symbols on the $\text{Ly}\alpha$ and $\text{Ly}\beta$ spectra represent regions possibly affected by imperfect correction for telluric absorption from the A and B bands, respectively. The black bar from $z = 5.725 - 5.79$ marks the longest dark trough present in $\text{Ly}\alpha$. The vertical dashed line at $z = 5.9134$ marks the inferred redshift of the host galaxy from metal lines.

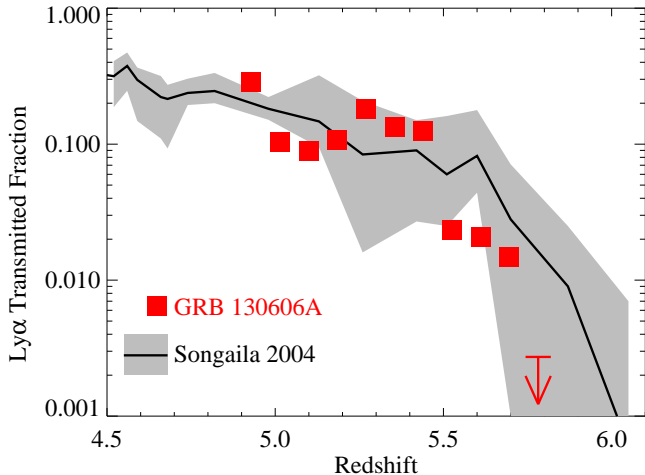


Figure 6. Transmission fraction of $\text{Ly}\alpha$ in 15 \AA bins from $1035 - 1200 \text{ \AA}$ (in the rest frame of GRB 130606A). The thick black line marks the mean values determined by Songaila (2004) with the gray region marking the range of observed values. The plotted upper limit is 3σ .

plotted symbols. The strong fluctuations in our measurements above and below the mean of the quasars are due to real cosmic variance caused by large-scale structure in the $\text{Ly}\alpha$ forest.

We convert our transmission measurements into an effective optical depth following the definition of Fan et al. (2006b) that

$$\tau_{\text{GP}}^{\text{eff}} = -\ln(\mathcal{T}), \quad (2)$$

where \mathcal{T} is the average transmission relative to the continuum. This is only an effective rather than true optical depth because transmission in a clumpy IGM with variable density and ionization is dominated by low-density regions (Songaila & Cowie 2002; Fan et al. 2002;

Oh & Furlanetto 2005). We compute this $\tau_{\text{GP}}^{\text{eff}}(\text{Ly}\alpha)$ in bins of size $\Delta z = 0.15$ relative to $\text{Ly}\alpha$ to facilitate direct comparison with the compilation of results from high-redshift quasars of Fan et al. (2006b). In addition, we compute the same statistic for $\text{Ly}\gamma$ and $\text{Ly}\beta$ in one and two bins, respectively. We use the same statistical correction as Fan et al. (2006b) for foreground $\text{Ly}\alpha$ absorption and the same conversion factors to determine $\tau_{\text{GP}}^{\text{eff}}(\text{Ly}\alpha)$ from $\tau_{\text{GP}}^{\text{eff}}(\text{Ly}\beta)$ and $\tau_{\text{GP}}^{\text{eff}}(\text{Ly}\gamma)$, so our results are calculated as consistently as possible with the quasar data. We show the points from GRB 130606A in Figure 7 and report the numbers in Table 2.

The data points from the GRB 130606A line of sight are generally consistent with the evolution of $\tau_{\text{GP}}^{\text{eff}}(\text{Ly}\alpha)$ seen along the quasar sight lines and fall within the observed range of variation, although our highest redshift bin has an optical depth on the high side relative to the quasar measurements. Our single $\text{Ly}\gamma$ point, covering $z = 5.70 - 5.85$, is the first using that tracer at $z < 6$ and implies a substantially higher $\tau_{\text{GP}}^{\text{eff}}(\text{Ly}\alpha) = 12.5$ than that measured from $\text{Ly}\alpha$ or $\text{Ly}\beta$. This was also seen by Fan et al. (2006b) at $z > 6$ in a very limited number of sightlines. $\text{Ly}\gamma$ measurements in the quasars are made difficult by the necessity of avoiding $\text{Ly}\delta$ at the blue end of the spectral window and the quasar's proximity zone at the red end. The interpretation of differences in $\tau_{\text{GP}}^{\text{eff}}$ determined from multiple proxies is complicated because the differing strengths of the transitions makes them differently sensitive to inhomogeneity in the IGM and requires comparison to numerical simulations. Recent work has focused on the statistics of dark pixels in the $\text{Ly}\alpha$ forest as a probe of the neutral fraction in the high-redshift universe to avoid dependence on models (McGreer et al. 2011). Fan et al. (2006b) emphasized that the quasar data at $z > 5.5$ show an acceleration in the evolution of the effective optical depth with redshift

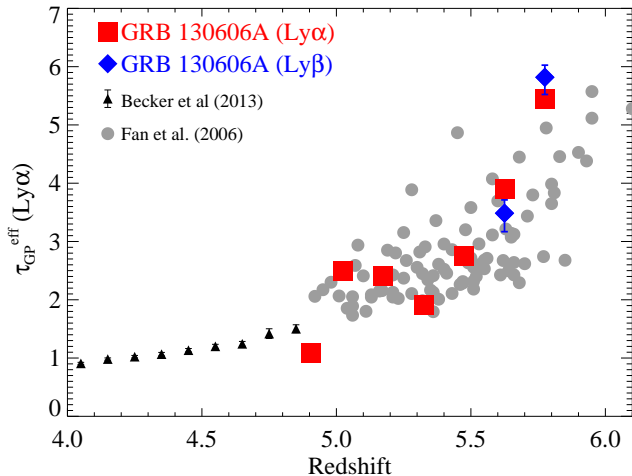


Figure 7. The effective optical depth to $\text{Ly}\alpha$, $\tau_{\text{GP}}^{\text{eff}}(\text{Ly}\alpha)$, computed in bins of width $\Delta z = 0.15$ in both $\text{Ly}\alpha$ and $\text{Ly}\beta$. Our estimate of $\tau_{\text{GP}}^{\text{eff}}$ from the $\text{Ly}\gamma$ absorption in the highest-redshift bin ($z=5.775$) is 12.5 and thus off the scale of the rest of the points on the plot. The error bars were computed from the extreme “Low” and “High” continuum models discussed in section 4.1 and represent bounds on the systematic uncertainties. The statistical errors are smaller than the plotted data points. The comparison points were measured in $\text{Ly}\alpha$ absorption of individual high-redshift quasars from Fan et al. (2006b) and a large sample of lower-redshift quasars from Becker et al. (2013).

relative to a power law extrapolation from data at lower redshifts (Songaila 2004; Becker et al. 2013), and that the scatter increases with redshift, possibly indicating that the tail end of reionization was a patchy process. The interpretation that there is an observed change in slope of $\tau_{\text{GP}}^{\text{eff}}$ associated with late reionization has been challenged by other studies (e.g., Becker et al. 2007).

4.1. Uncertainties

We now consider the sources of uncertainty in these optical depth measurements. We do not list formal error bars in Table 2 because the statistical errors are completely negligible and dominated by systematics. To demonstrate this point, we note that the median error bar per 1.38 \AA spectral pixel in the GMOS data between $z_{\text{Ly}\alpha}$ of 5 and 6 is 0.8% of the unabsorbed continuum. The large redshift bins we use to compare to the results of Songaila (2004) and Fan et al. (2006b) then average over many such pixels ($\Delta z=0.15$ is ~ 132 pixels). Another check on our errors is to compare our two independent spectra from different instruments. Results from both MMT and GMOS are given in Table 2 and are mostly similar, except for the darkest part of the $\text{Ly}\alpha$ absorption between redshifts 5.7 and 5.8, where the MMT data show more transmission. This is caused by the extra bit of flux visible near 8150 \AA in Figure 1. This effect was caused by inadequate flat fielding and removal of the slit function in the MMT data leading to uneven background levels along the slit. It results in a slight excess of flux per pixel after background subtraction that is only visible near zero flux levels when the data are binned up. The exact amount of this positive flux was found to vary depending the exact background apertures chosen. We trust the GMOS data much more due to their significantly higher S/N and our ability to check with the nod-and-shuffle reduction, which has much better control

over the flat-fielding and sky subtraction uncertainties at flux levels near zero.

Our results are presented as transmission fractions, so we also need to examine our assumptions about the proper level of the unabsorbed continuum. We have been using our best-fit power law so far in this analysis. In section 2, we noted that the continuum did appear to be curved relative to a single power law. Multiband photometry extending to the NIR reported by the RATIR and GROND collaborations (Butler et al. 2013; Afonso et al. 2013) implies a bluer power law than the flatter continuum we have fit to our data over a more limited wavelength range. These observations can easily be reconciled by a small amount of dust producing curvature in the spectral energy distribution given that our observations are at rest-frame wavelengths $< 1450 \text{ \AA}$. However, we will demonstrate that our results are robust for any reasonable value for the true shape of the continuum.

We show two extreme hypothetical alternative continuum shapes in Figure 1 as dashed lines. All assumed continuum shapes have to be constrained to pass near the actual observed continuum near 8650 \AA . In addition, there is a peak in the IGM transmission near 7150 \AA that the true unabsorbed continuum must pass above, which sets a limit on how red the continuum can be. This power-law slope is shown by the lower dashed line on the figure. As a maximally blue model, we take a power law with a slope as different from the best fit model as the maximally red one, but in the opposite direction from the best fit, and also constrain it to match the data near 8650 \AA . We normalize the GMOS data by both of these extreme models and computed the transmission fraction in the same redshift bins as above. We list the results with these alternative continuum normalizations (called “Low” and “High”) for two redshift bins in Table 2. Even in our bluest bins, at $z \approx 5$, the difference in $\tau_{\text{GP}}^{\text{eff}}(\text{Ly}\alpha)$ is only ~ 0.1 . At higher redshift, closer in wavelength to where the continua are normalized, the effect is even smaller. In part, this is because $\tau_{\text{GP}}^{\text{eff}}$ depends only logarithmically on the continuum normalization. We emphasize that these alternative normalizations are far larger than anything motivated by the data and yet they do not materially affect the results. The maximal effects on the GRB 130606A data points in Figures 6 and 7 induced by these choices of continuum slope are smaller than the points on the plots.

We conclude that the uncertainties in our optical depth measurements are negligible compared to the dominant systematics in interpretation caused by theoretical uncertainties and cosmic variance along different lines of sight. In particular, these measurements would benefit from an improved theoretical understanding of the differences between $\tau_{\text{GP}}^{\text{eff}}(\text{Ly}\alpha)$ measured from the different Lyman series lines.

4.2. Dark GP Trough

We examine our spectra for continuous regions of extremely high opacity and find that there is no detectable $\text{Ly}\alpha$ transmission in the redshift range of $z=5.71-5.83$, with a 3σ upper limit of $\mathcal{T}_{\text{Ly}\alpha} \lesssim 0.2\%$, or $\tau_{\text{GP}}^{\text{eff}}(\text{Ly}\alpha) > 6.4$. This is comparable in width and optical depth to the lowest-redshift Gunn-Peterson (Gunn & Peterson 1965) troughs previously claimed,

Table 2
GRB 130606A Ly α Transmission

Redshift Range	Line	Spectrum ^a	Continuum ^b	Transmission	$\tau_{\text{GP}}^{\text{eff}}(\text{Ly}\alpha)$
4.86–4.95 ^c	Ly α	G	BF	0.406	0.90
4.95–5.10	Ly α	G	BF	0.089	2.41
4.95–5.10	Ly α	G	L	0.099	2.31
4.95–5.10	Ly α	G	H	0.084	2.48
5.10–5.25	Ly α	G	BF	0.100	2.30
5.13–5.25 ^d	Ly α	M	BF	0.109	2.22
5.25–5.40	Ly α	G	BF	0.168	1.78
5.25–5.40	Ly α	M	BF	0.164	1.81
5.40–5.55	Ly α	G	BF	0.079	2.54
5.40–5.55	Ly α	M	BF	0.081	2.52
5.55–5.70	Ly α	G	BF	0.022	3.80
5.55–5.70	Ly α	M	BF	0.021	3.88
5.55–5.70	Ly β	G	BF	0.228	3.33
5.70–5.85	Ly α	G	BF	0.005	5.29
5.70–5.85	Ly α	G	L	0.005	5.24
5.70–5.85	Ly α	G	H	0.005	5.29
5.70–5.85	Ly α	M	BF	0.016	4.13
5.70–5.85	Ly β	G	BF	0.074	5.85
5.70–5.85	Ly γ	G	BF	0.059	12.5
Darkest trough					
5.71–5.83	Ly α	G	BF	$\lesssim 0.0017$	$\gtrsim 6.36$
5.71–5.83	Ly β	G	BF	0.062	6.22
5.71–5.83	Ly γ	G	BF	0.026	13.0
5.725–5.79	Ly α	G	BF	$\lesssim 0.0022$	$\gtrsim 6.13$
5.725–5.79	Ly β	G	BF	0.019	8.86
5.725–5.79	Ly γ	G	BF	0.023	16.6

^a G=Gemini, M=MMT

^b Continuum normalization: BF= Best fit, L = Low, H=High

^c Lower redshift limit truncated to avoid Ly β absorption from host

^d Lower redshift limit set by spectral range

which were identified by Fan et al. (2006b) in the quasars SDSS J104845.05+463718.3 (Fan et al. 2003) and SDSS J125051.93+313021.9 (Fan et al. 2006a). However, there are clear spikes of Ly β transmission at the ends of this redshift interval, including the interesting peak near $z=5.803$ noted previously to be almost coincident in redshift with a foreground absorber, so we also define a narrower redshift range of $z=5.725-5.79$ to isolate the darkest part of the trough. This more restricted interval is the one marked with a black bar on Figure 5. The \mathcal{T} and $\tau_{\text{GP}}^{\text{eff}}(\text{Ly}\alpha)$ measurements for these two interval definitions are tabulated in Table 2.

Despite the lack of detectable Ly α , some flux is present in the Ly β and Ly γ windows, indicating that the redshift interval is far from opaque and still highly ionized. The transmission of Ly γ over the core redshift range implies that $\tau_{\text{GP}}^{\text{eff}}(\text{Ly}\alpha)$ is ~ 17 .

4.3. Neutral fraction in the IGM

The afterglow spectra of GRBs can also be used to probe the neutral fraction of the IGM (Miralda-Escude 1998; Barkana & Loeb 2004). If a high-redshift GRB occurs when the universe still contains a substantial fraction of neutral hydrogen, the red damping wing of this material will affect the shape of the cutoff in flux at Ly α . Totani et al. (2006) have searched for such an effect in the spectrum of the $z=6.295$ GRB 050904 and found a best fit consistent with zero neutral hydrogen, although their analysis was hampered by the strong DLA of the host galaxy. Patel et al. (2010) have also performed an analysis on the $z=6.733$ GRB 080913 and again found a null result. The much lower $\log(N_{\text{HI}})$ we determine here

than for GRB 050904 and the higher S/N of our data relative to the spectrum of GRB 080913 allow us a cleaner test, although the neutral fraction is not expected to be sufficiently high to be detectable at this lower redshift given the limits on Ly α opacity discussed above.

We use the approximations of Miralda-Escude (1998) to model the IGM neutral density as a constant over the redshift range of interest. A pure IGM fit to the Ly α cutoff in the GMOS spectrum is a significantly worse fit than the single absorber model from Section 3. In addition, minima in the Ly β and Ly γ absorption spectra at the host redshift (Figure 5) demonstrate the need for at least some absorption from the host galaxy. A combined fit with a host galaxy absorber (fixed to the redshift of the metal lines) along with the IGM model can fit the data as long as the IGM neutral fraction (x_{HI}) is below 0.05, but is not required by the data. We conclude that our spectra are consistent with zero neutral fraction and $x_{\text{HI}} < 0.11$ at the 2σ level (Figure 8). However, allowing more realistic models than a simple constant neutral density in the IGM makes the interpretation of Ly α damping wings more problematic and significantly relaxes these constraints (Mesinger & Furlanetto 2008; McQuinn et al. 2008).

We note that although most GRB host galaxies are DLAs (Jakobsson et al. 2006), two out of the three highest redshift events with good measurements of the host hydrogen columns have $\log(N_{\text{HI}}) < 20$ (GRBs 130606A and 080913), which may bode well for the detectability of the red damping wing effect in the future at higher redshift. An evolution in the $\log(N_{\text{HI}})$ values observed in GRB afterglow spectra would also have important im-

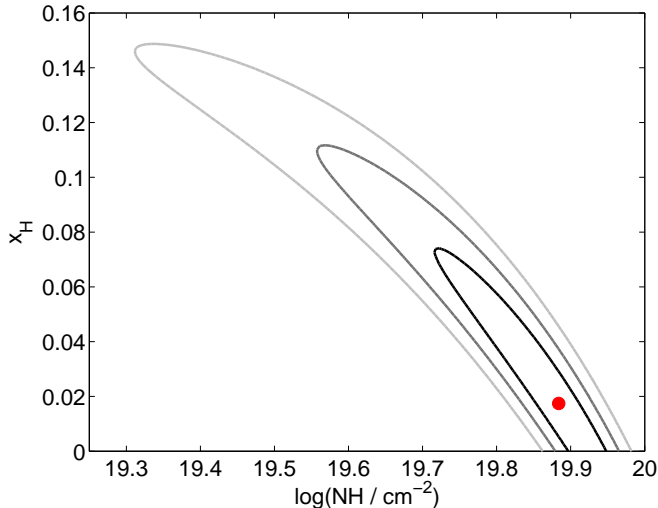


Figure 8. Contours (1, 2, and 3σ) of fits to the red wing of $\text{Ly}\alpha$ absorption when a simple model with constant x_{HI} in the IGM (Miralda-Escude 1998) is allowed in addition to an absorber at the host redshift with a column density of $\log(N_{\text{HI}})$. Models treating IGM inhomogeneity more realistically will significantly relax these constraints (Mesinger & Furlanetto 2008; McQuinn et al. 2008), but the best fit will still be consistent with zero neutral fraction.

plications for reionization. Chen et al. (2007) have used the distribution of $\log(N_{\text{HI}})$ values observed in GRB afterglow spectra as a proxy to measure the escape fraction of UV ionizing photons from star-forming galaxies. If the GRB host galaxy $\log(N_{\text{HI}})$ distribution really is lower at higher redshift, then the higher escape fractions would imply that star-forming galaxies can more efficiently reionize the universe. Data from more lines of sight at these high redshifts are necessary to test this hypothesis.

5. CONCLUSIONS

We have presented high S/N spectra of the optical afterglow of GRB 130606A at $z=5.9134$, the first high-redshift afterglow to have a dataset of similar quality for IGM studies to those published for individual high- z quasars, although our spectral resolution was not as high as in the best quasar datasets (e.g., White et al. 2003). For comparison, we estimate that the continuum magnitude at the time of the GMOS observations was ~ 19.6 mag (Perley & Cenko 2013; Afonso et al. 2013), or $M_{1250\text{\AA}}^{\circ} \approx -27$ mag (AB). This is comparable to the most luminous quasars known at similar redshifts (Fan et al. 2006b) and we were able to obtain 1.3 hr of spectroscopy with the 6.5-m MMT and 2 hr with the 8-m Gemini-N telescope.

These observations represent the first dataset on the evolution of the IGM opacity at these redshifts using a tracer other than quasars, which Mesinger (2010) has argued are sufficiently biased tracers of large-scale structure that they will overestimate the degree of ionization of the IGM. It is therefore reassuring that the general trend of the quasar observations is reproduced in our dataset, although an individual sightline is of limited utility for making firm conclusions because of cosmic variance. Once we have obtained a sample of GRB afterglow spectra at high redshift, it will be interesting to compare the statistics of $\text{Ly}\alpha$ absorption using both tracers.

We also find an extended region of $\text{Ly}\alpha$ absorption from $z=5.71$ to 5.83 , similar to the lowest-redshift Gunn-Peterson troughs found in quasar absorption spectra, over which we place a 3σ upper limit of 0.2% on the $\text{Ly}\alpha$ transmitted fraction, although $\text{Ly}\beta$ and $\text{Ly}\gamma$ are not completely absorbed. The pixel-scale statistics (e.g., McGreer et al. 2011) of dark regions in $\text{Ly}\alpha$ absorption windows such as this in a larger sample of GRB afterglows will offer a complementary view of reionization to the studies of quasars.

In addition, we have identified numerous metal absorptions on the bright GRB afterglow continuum at wavelengths redward of $\text{Ly}\alpha$ at the host redshift, due to both the IGM and the ISM of the host galaxy. A metal absorption system at $z=5.806$ appears to be correlated with a region of slightly enhanced transmission in the $\text{Ly}\beta$ and $\text{Ly}\gamma$ forests. We have used the host ISM absorption lines to bracket the gas phase abundances for this star-forming galaxy at $z=5.913$ between $[\text{Si}/\text{H}] \gtrsim -1.7$ and $[\text{S}/\text{H}] \lesssim -0.5$. The low hydrogen column density in this host galaxy ($\log(N_{\text{HI}}) = 19.93 \pm 0.07$) as well as that of the $z=6.7$ GRB 080913 may be evidence for an evolving escape fraction for UV photons from star-forming galaxies at high redshift.

We thank the Gemini and MMT staffs for their assistance in obtaining these observations. The Berger GRB group at Harvard is supported by the National Science Foundation under Grant AST-1107973 and by NASA/*Swift* AO8 grant NNX13AJ64G. Based in part on observations obtained under Program ID GN-2013A-Q-39 (PI: Cucchiara) at the Gemini Observatory, which is operated by the Association of Universities for Research in Astronomy, Inc., under a cooperative agreement with the NSF on behalf of the Gemini partnership: the National Science Foundation (United States), the Science and Technology Facilities Council (United Kingdom), the National Research Council (Canada), CONICYT (Chile), the Australian Research Council (Australia), Ministério da Ciência, Tecnologia e Inovação (Brazil) and Ministerio de Ciencia, Tecnología e Innovación Productiva (Argentina). Some observations reported here were obtained at the MMT Observatory, a joint facility of the Smithsonian Institution and the University of Arizona.

Facilities: Gemini:Gillett (GMOS-N), MMT (Blue Channel Spectrograph)

REFERENCES

- Afonso, P., Kann, D. A., Nicuesa Guelbenzu, A., et al., GRB Coordinates Network, 14807, 1
 Asplund, M., Grevesse, N., Sauval, A. J., & Scott, P. 2009, *ARA&A*, 47, 481
 Barkana, R., & Loeb, A. 2004, *ApJ*, 601, 64
 Barthelmy, S., et al., GRB Coordinates Network, 14819, 1
 Becker, G. D., Rauch, M., & Sargent, W. L. W. 2007, *ApJ*, 662, 72
 Becker, G. D., Sargent, W. L. W., Rauch, M., & Calverley, A. P. 2011, *ApJ*, 735, 93
 Becker, G. D., Hewett, P. C., Worseck, G., & Prochaska, J. X. 2013, *MNRAS*, 430, 2067
 Becker, R. H., Fan, X., White, R. L., et al. 2001, *AJ*, 122, 2850
 Berger, E., Penprase, B. E., Cenko, S. B., et al. 2006, *ApJ*, 642, 979

- Butler, N., Watson, A. M., Kuttyrev, A., et al., GRB Coordinates Network, 14799, 1
- Castro-Tirado, A. J., Sánchez-Ramírez, R., Jelinek, M., et al. 2013a, GRB Coordinates Network, 14790, 1
- Castro-Tirado, A. J., Sánchez-Ramírez, R., Gorosabel, J., et al. 2013b, GRB Coordinates Network, 14796, 1
- Chen, H.-W., Prochaska, J. X., & Gnedin, N. Y. 2007, *ApJ*, 667, L125
- Cucchiara, A., Levan, A. J., Fox, D. B., et al. 2011, *ApJ*, 736, 7
- Erb, D. K., Shapley, A. E., Pettini, M., et al. 2006, *ApJ*, 644, 813
- Fan, X., Narayanan, V. K., Strauss, M. A., et al. 2002, *AJ*, 123, 1247
- Fan, X., Strauss, M. A., Schneider, D. P., et al. 2003, *AJ*, 125, 1649
- Fan, X., Strauss, M. A., Richards, G. T., et al. 2006a, *AJ*, 131, 1203
- Fan, X., Strauss, M. A., Becker, R. H., et al. 2006b, *AJ*, 132, 117
- Filippenko, A. V. 1982, *PASP*, 94, 715
- Furlanetto, S. R., & Loeb, A. 2003, *ApJ*, 588, 18
- Gallerani, S., Salvaterra, R., Ferrara, A., & Choudhury, T. R. 2008, *MNRAS*, 388, L84
- Glazebrook, K., & Bland-Hawthorn, J. 2001, *PASP*, 113, 197
- Greiner, J., Krühler, T., Fynbo, J. P. U., et al. 2009, *ApJ*, 693, 1610
- Gunn, J. E., & Peterson, B. A. 1965, *ApJ*, 142, 1633
- Haislip, J. B., Nysewander, M. C., Reichart, D. E., et al. 2006, *Nature*, 440, 181
- Hinshaw, G., Larson, D., Komatsu, E., et al. 2012, arXiv:1212.5226
- Hook, I. M., Jørgensen, I., Allington-Smith, J. R., et al. 2004, *PASP*, 116, 425
- Jakobsson, P., Fynbo, J. P. U., Ledoux, C., et al. 2006, *A&A*, 460, L13
- Jelinek, M., Gorosabel, J., Castro-Tirado, A. J., et al. 2013, GRB Coordinates Network, 14782, 1
- Kawai, N., Kosugi, G., Aoki, K., et al. 2006, *Nature*, 440, 184
- Lamb, D. Q., & Reichart, D. E. 2000, *ApJ*, 536, 1
- Laskar, T., Zauderer, A., & Berger, E. 2013, GRB Coordinates Network, 14817, 1
- Lunnan, R., Drout, M., Chornock, R., & Berger, E. 2013, GRB Coordinates Network, 14798, 1
- Mannucci, F., Cresci, G., Maiolino, R., et al. 2009, *MNRAS*, 398, 1915
- McGreer, I. D., Mesinger, A., & Fan, X. 2011, *MNRAS*, 415, 3237
- McQuinn, M., Lidz, A., Zaldarriaga, M., Hernquist, L., & Dutta, S. 2008, *MNRAS*, 388, 1101
- Mesinger, A. 2010, *MNRAS*, 407, 1328
- Mesinger, A., & Furlanetto, S. R. 2008, *MNRAS*, 385, 1348
- Miralda-Escude, J. 1998, *ApJ*, 501, 15
- Nagayama, T. 2013, GRB Coordinates Network, 14784, 1
- Oh, S. P. 2002, *MNRAS*, 336, 1021
- Oh, S. P., & Furlanetto, S. R. 2005, *ApJ*, 620, L9
- Patel, M., Warren, S. J., Mortlock, D. J., & Fynbo, J. P. U. 2010, *A&A*, 512, L3
- Perley, D. A., & Cenko, S. B. 2013, GRB Coordinates Network, 14804, 1
- Price, P. A., Songaila, A., Cowie, L. L., et al. 2007, *ApJ*, 663, L57
- Prochaska, J. X. 2006, *ApJ*, 650, 272
- Prochaska, J. X., Chen, H.-W., & Bloom, J. S. 2006, *ApJ*, 648, 95
- Prochaska, J. X., Chen, H.-W., Bloom, J. S., et al. 2007, *ApJS*, 168, 231
- Prochaska, J. X., Dessauges-Zavadsky, M., Ramirez-Ruiz, E., & Chen, H.-W. 2008, *ApJ*, 685, 344
- Rafelski, M., Wolfe, A. M., Prochaska, J. X., Neeleman, M., & Mendez, A. J. 2012, *ApJ*, 755, 89
- Salvaterra, R., Della Valle, M., Campana, S., et al. 2009, *Nature*, 461, 1258
- Savage, B. D., & Sembach, K. R. 1996, *ARA&A*, 34, 279
- Schlafly, E. F., & Finkbeiner, D. P. 2011, *ApJ*, 737, 103
- Schmidt, G. D., Weymann, R. J., & Foltz, C. B. 1989, *PASP*, 101, 713
- Songaila, A. 2004, *AJ*, 127, 2598
- Songaila, A., & Cowie, L. L. 2002, *AJ*, 123, 2183
- Tanvir, N. R., Fox, D. B., Levan, A. J., et al. 2009, *Nature*, 461, 1254
- Tanvir, N. R., Levan, A. J., Fruchter, A. S., et al. 2012, *ApJ*, 754, 46
- Thöne, C. C., Fynbo, J. P. U., Goldoni, P., et al. 2013, *MNRAS*, 428, 3590
- Totani, T., Kawai, N., Kosugi, G., et al. 2006, *PASJ*, 58, 485
- Ukwatta, T. N., Barthelmy, S. D., Gehrels, N., et al. 2013, GRB Coordinates Network, 14781, 1
- van Dokkum, P. G. 2001, *PASP*, 113, 1420
- Virgili, F. J., Mundell, C. G., & Melandri, A. 2013, GRB Coordinates Network, 14785, 1
- Vreeswijk, P. M., Ledoux, C., Smette, A., et al. 2007, *A&A*, 468, 83
- White, R. L., Becker, R. H., Fan, X., & Strauss, M. A. 2003, *AJ*, 126, 1
- Woosley, S. E., & Bloom, J. S. 2006, *ARA&A*, 44, 507
- Xu, D., Malesani, D., Schulze, S., et al. 2013, GRB Coordinates Network, 14783, 1
- Xu, D., Malesani, D., Schulze, S., et al. 2013, GRB Coordinates Network, 14816, 1